

Active Power Filter Control Strategy with Implicit Closed-Loop Current Control

V. Arun Kumar^{*1} Department of Electrical & Electronics Engineering
 Syed Karimulla^{*2} Department of Electrical & Electronics Engineering
 P. G Scholar Student member IEEE¹, Associate professor²
 Al-Habeeb college of Engineering and Technology

Abstract—A simple indirect sensorless control strategy for an active power filter (APF) application has been Proposed. The concepts are exemplarily presented to control a modified APF structure with a battery energy storage considered R-L Load. The main advantage over other control strategies is the achieved excellent simplicity-to-performance ratio. The proposed control strategies are based on the concept of virtual impedance emulation to provide high power factor in a system. To validate the operating principle, a single-phase low-power Simulation circuit has been built using Matlab/Simulink Software. This Simulation Circuit operates at a remarkably low switching frequency of 5 kHz with a suitable control strategy.

Index Terms—Active power filter (APF), dc-ac converters, implicit control, Battery Storage, sensorless control techniques.

I. INTRODUCTION

NONLINEAR loads connected to electric energy distribution networks generate harmonic pollution. Such nonlinear loads drain currents with varying degree of harmonic contents. The harmonic current components do not represent useful active power due to the frequency mismatch with the grid voltage. However, the circulation of harmonic currents through feeders and protective network elements produces Joule losses and electromagnetic emissions that might interfere with other devices connected to the distribution network. This affects the electrical performance of control and communication systems involved with the protective elements. Several other harmful effects are observed as presented in [1] and [2].

A remedy to the harmonic current injection problem is to connect passive, active [3], [4], or hybrid [5] filters in parallel with the loads. These are named shunt active power filters (APFs) [6], [7]. APFs are circuits based on switched power semiconductors (typically employing voltage-source inverters) that inject opposed phase harmonic currents at the point of common coupling (PCC). This results in the whole nonlinearload- plus-APF system emulating a nearly resistive load behavior at the PCC terminals. Power transmission in the network is, thus, optimized, and all nonlinear load low-frequency-harmonic electromagnetic compatibility issues are diminished.

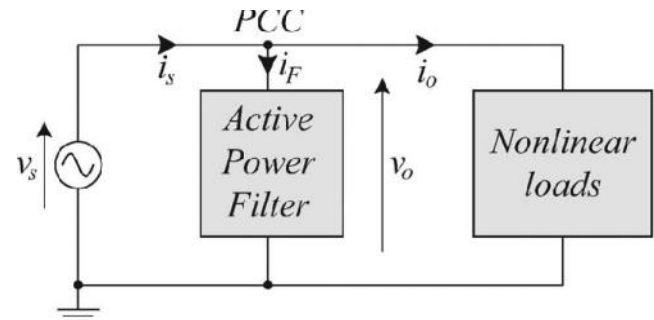


Fig. 1. APF connected in parallel with the loads—shunt-type APF. The filter current i_F supplies the load harmonic current contents.

Two tasks are crucial to an APF to perform well its function, namely, the generation of appropriate current references and the ability to rapidly follow the reference current signals. Thus, typical shunt APFs use the error signal generated by the comparison of measured currents with the references. The main control objective is to minimize such error. Finally, the employed controllers generate the modulation signals to the inverter power section. Generally, error minimization is achieved through two different types of methods, the direct control methods or the indirect ones. In the direct control methods, the required compensation inverter current reference is the one generated within the control algorithm. On the other hand, the indirect control methods generate the APF current reference indirectly, i.e., by causing that the APF-plus-nonlinear-load currents follow sinusoidal reference current signals in phase with the PCC voltages. Therefore, using the scheme shown in Fig. 1

$$i_F^* = i_s^* - i_o = i_{s,\text{nonactive}}^* - \sum_{h=1}^{N_{h,\text{max}}} i_{o(h)} \quad (1)$$

where i_F^* and i_s^* are the APF and the PCC reference currents, respectively, $i_{s,\text{nonactive}}^*$ is the nonactive current component of the mains current i_s , and $i_{o(h)}$ represents the load-side current harmonics of order h . This condition guarantees that the correct inverter compensation current is injected even if the mains voltage presents harmonic distortion. The indirect control methods are typically easier to implement since only the input variables (currents and voltages) are measured. On the other hand, the direct methods require sophisticated reference generation mechanisms.

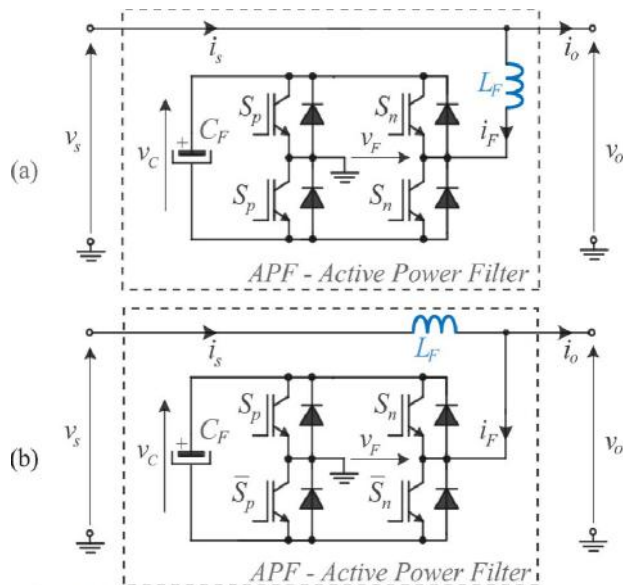


Fig. 2. (a) Typical single-phase APF system architecture. (b) APF architecture used in this work.

Fig. 2(a) shows a conventional APF system architecture where the smoothing inductor L_F is series connected to the voltage-source inverter. The compensation opposite phase load harmonic currents flow through the inductor, generating the according harmonic voltages across the inductor in this architecture.

Assuming a purely sinusoidal mains voltage v_s results in that the voltage drop across the inductor is generated by the inverter output voltage. Thus, the bandwidth of the modulation signal must be compatible with the voltage harmonics that are to be generated since the modulation signal is directly proportional to such voltage. In practice, considering that up to the 50th-order harmonic component must be compensated in specifications such as that given in the IEEE 519 standard and the IEC 61000-3 series, i.e., 2.5 kHz in a 50-Hz network, leads to the need to employ high switching frequency f_c . Carrier frequencies above $f_c > 25$ kHz would be desirable, and the local averaging method would provide proper results to model the system.

A solution to this challenge is to consider the APF system architecture shown in Fig. 2(b) [8]–[11]. The smoothing inductor L_F is now placed in series with the network and not with the inverter as usual. The dc-link capacitor C_F requirements are approximately the same as in the standard APF configuration.

The disadvantages of this architecture are that the inductor carries the full load current, except the harmonics, the PCC voltage v_o is now switched (it requires a low-pass filter prior to the load), and the load voltage can be distorted due to load current harmonic components. Another aspect is that the presence of L_F limits the rate of change of the load current. However, this APF structure implies an advantage from the APF control strategy viewpoint. The inductor current reference is now sinusoidal and in phase with the mains voltage as is the APF modulating signal $m(t)$. Therefore, the inductor current becomes independent from the harmonic currents of the load. It follows that

$$\bar{v}_o = \bar{v}_F = \hat{V} \cdot \sin(\omega_1 \cdot t + \varphi) \quad (2)$$

where \bar{x} represents the local average value of x during a carrier period, \hat{V} is the peak value of the mains voltage, and ω_1 is the mains voltage angular frequency. In this context, the present work proposes novel indirect APF control methods to be applied in the modified shunt APF structure shown in Fig. 2(b).

The proposed control strategy is much simpler to implement than conventional strategies, such as the ones listed in the following. Perhaps, the most widespread method is the average current mode control [12], which presents an outer voltage control loop and an internal current control loop. Large control bandwidths are typically required with this approach.

Hysteresis current control is also employed and demands a single outer voltage control loop to generate the current references.

This scheme leads to very fast dynamics but brings all disadvantages inherent to variable switching frequency. Examples of digital control strategies using intern model principles are the adaptive [13] and the dead-beat control. One of the main control challenges faced in all these strategies is the generation of current references. Among the theories to compute the compensation reference current are the $p-q$ theory [14], [15], the synchronic reference frame [16], the discrete Fourier transform [17], adaptive neural networks [1], [13], and Lyapunov-function-based control [18], [6]. These techniques, while having an acceptable performance for achieving input unity power factor, are relatively complex to implement. In the case of digital programming, powerful digital signal processors (DSPs) are required in addition to analog-to-digital converters, phase-locked loops, and other demanding software tasks.

Novel APF control indirect strategies are proposed here as alternative to the cited techniques. These novel indirect methods are based on the concept of virtual impedance emulation through inverters to achieve unity input power factor. A key feature is that either mains-side current or voltage sensor is used, leading to sensorless strategies. The APF implicit current reference does not contain high-order harmonic components to ensure unity power factor at the mains, and thus, the control function is greatly simplified, leading to the control methods derived in Section II. The system is theoretically analyzed in Section III. The strategies can be implemented with both analog and digital electronics, demanding minimum hardware and data processing capabilities. The achieved performance is similar or superior to that attained with conventional strategies as shown through the simulation and experimental results given in Sections IV and V. The main contribution of this work lies on the use of very simple implicit current controllers to control an APF.

II. APF INDIRECT CONTROL STRATEGY CONCEPTS

A. Current Sensorless Strategy

Applying Kirchoff's second law to the circuit in Fig. 1 gives

$$v_s - L_F \cdot \frac{di_s}{dt} - \underbrace{(s_p - s_n)}_{=s_F} \cdot v_c = 0 \quad (3)$$

where s_p and s_n are the switching functions for switches S_p and S_n , respectively. These are defined as +1 if a switch is closed and 0 when it is off. The resulting switching function for the filter comprehends both of these into $s_F = s_p - s_n$. The switching signals are generated by a proper modulation scheme.

For the case at hand, phase-shifted pulsewidth modulation (PWM) is adopted. The high-frequency (HF) harmonics are typically eliminated with filters, and the following analysis considers only the low-frequency behavior of the circuit. This is achieved with the definition of the local average value \bar{x} of the quantities within a switching period T_s . Applying this definition to the APF switching function leads to

$$\bar{s}_F = \frac{1}{T_s} \int_{t-T_s}^t s_F dt = d_F \quad (4)$$

where d_F is the resulting APF duty cycle. This is to be generated by the control strategy. Applying (4) to (3) results in

$$\bar{v}_s - L_F \frac{d\bar{i}_s}{dt} - d_F \bar{v}_c = 0. \quad (5)$$

Assuming that a unity input power factor is to be achieved, the system should emulate a resistive behavior. Thus

$$\bar{i}_s = \frac{\bar{v}_s}{R_e^*} \quad (6)$$

where R_e^* is the desired resistance value.

The APF dc-link voltage is controlled with a variable v_m defined as

$$v_m = \frac{kV_c^*}{R_e^*} \quad (7)$$

where k is a gain and V_c^* is the dc-link voltage reference.

Isolating R_e^* in (7) and using it in (5) give

$$\bar{v}_s - L_F \frac{d}{dt} \left(\frac{\bar{v}_s v_m}{kV_c^*} \right) - d_F \bar{v}_c = 0. \quad (8)$$

Assuming a purely sinusoidal \bar{v}_s leads to

$$\frac{d}{dt}(\bar{v}_s) = -\omega^2 \int \bar{v}_s dt \quad (9)$$

where ω is the sinus angular frequency.

The control signal v_m is assumed constant at steady state. Thus, (8) is rewritten as

$$\bar{v}_s + \frac{\omega^2 L_F}{kV_c^*} \int (\bar{v}_s v_m) dt - d_F \bar{v}_c = 0. \quad (10)$$

Defining

$$k_1 = \frac{\omega^2 L_F}{kV_c^*} \quad (11)$$

and replacing it in (9) result in

$$d_F = \frac{\bar{v}_s}{\bar{v}_c} + \frac{k_1}{\bar{v}_c} \int (\bar{v}_s v_m) dt. \quad (12)$$

The resulting control block diagram is shown in Fig. 3. This control strategy is simple and does not require complex computations for the generation of references. The phase-shifted

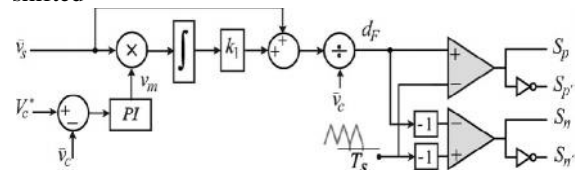


Fig. 3. Block diagram for the current sensorless control strategy

Based on (12).

PWM leads to the output of the inverter generating a voltage with twice the carrier frequency and with reduced current ripple. The procedure to determine the duty cycle described earlier is input current sensorless and has the advantage of only measuring the input and the dc-link voltages to generate the control signal.

B. Voltage Sensorless Strategy

Similar to the input current sensorless strategy, an input voltage sensorless strategy is derived in the following.

Replacing v_s from (6) in (5) gives

$$R_e^* \bar{i}_s - L_F \frac{d\bar{i}_s}{dt} - d_F \bar{v}_c = 0. \quad (13)$$

During sinusoidal steady state

$$\frac{d}{dt}(\bar{i}_s) = -\omega^2 \int \bar{i}_s dt. \quad (14)$$

Defining the dc-link voltage control signal as

$$v_m = \frac{R_s V_c^*}{R_e^*} \quad (15)$$

where R_s is the current measurement gain, and substituting the aforementioned relations into (13) lead to

$$V_c^* R_s \frac{\bar{i}_s}{v_m} + \omega^2 L_F \int \bar{i}_s dt - d_F \bar{v}_c = 0. \quad (16)$$

Defining gain k_2 as

$$k_2 = \frac{L_F \omega^2}{R_s V_c^*} \quad (17)$$

and dividing (16) by $V_c^* R_s$ finally give the duty cycle

$$\frac{d_F}{R_s V_c^*} = \frac{\bar{i}_s}{v_m \bar{v}_c} + \frac{k_2}{\bar{v}_c} \int \bar{i}_s dt. \quad (18)$$

The voltage sensorless control strategy based on (18) is implemented with the block diagram shown in Fig. 4. The strategy is straightforward and similar from the practical implementation aspects to the current sensorless one. The advantage of this approach over the current sensorless one is that overcurrent protection techniques are easier to implement with the current measurement. However, the semiconductor currents are not directly measured in neither approaches.

Suitable current protection for insulated-gate bipolar transistors can be implemented through high-performance gate drivers, low-precision current sensors, and the measurement of the dc-side current.

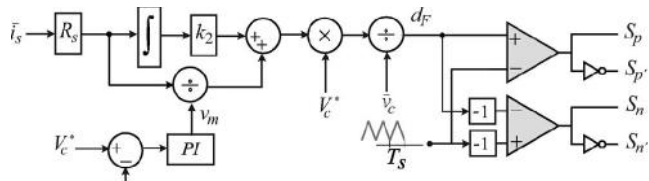


Fig. 4. Block diagram for the voltage sensorless control based on (18).

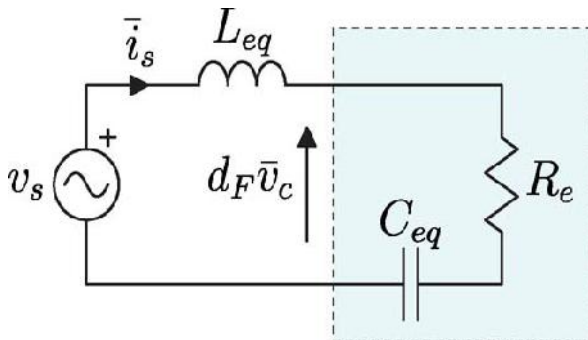


Fig. 5. Equivalent circuit for the control strategy to emulate virtual capacitance C_{eq} .

III. THEORETICAL ANALYSIS OF THE PROPOSED INDIRECT CONTROL SENSORLESS STRATEGIES

This section presents theoretical analyses regarding the equivalent circuit observed from the mains and the equivalence between the proposed control technique and a control strategy that uses conventional feedback control theory with a resonant controller to obtain close-to-unity power factor. Furthermore, a general stability analysis is presented.

A. Equivalent-Circuit-Based Analysis

Considering the low-frequency behavior of the proposed APF configuration and a constant dc-link voltage $v_c = V^*$ $c = Vc$ leads to

$$v_s = L_F \frac{di_s}{dt} + s_F v_c \cong L_F \frac{d\bar{i}_s}{dt} + d_F V_c. \quad (19)$$

Replacing the duty-cycle calculation function defined in (18) into (19) gives

$$v_s \cong \underbrace{L_F}_{=L_{eq}} \frac{d\bar{i}_s}{dt} + \underbrace{\frac{R_s V_c}{v_m}}_{=R_e} \bar{i}_s + \underbrace{\omega^2 L_F}_{=\frac{1}{C_{eq}}} \int \bar{i}_s dt \quad (20)$$

where the parameters L_{eq} , R_e , and C_{eq} are the equivalent circuit elements that model the controlled system. The equivalent circuit is shown in Fig. 5. This expression shows that the equivalent input impedance of the active filter with the proposed control strategy includes a series connection of a resistance R_e and a capacitance C_{eq} . The resistance is responsible for the active power transference to the load, whereas the series capacitance compensates for the filter inductance L_F . A frequencydomain analysis is applied to the equivalent circuit. The first step is to define the reactive

impedances $jX_L = j L_{eq}$ and $-jX_C = -j/(C_{eq})$, with $j = -1$. Computing the total equivalent series impedance gives

$$jX_L - jX_C = j\omega L_F - \frac{j\omega^2 L_F}{\omega} = 0 \quad (21)$$

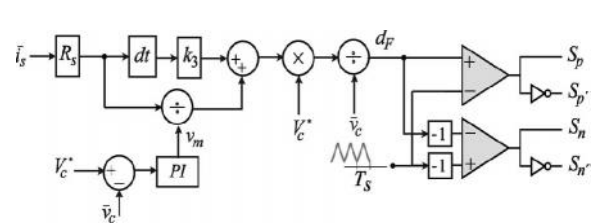


Fig. 6. Block diagram for a control strategy based on the emulation of a virtual negative inductance to cancel the effects of L_F and guarantee close-to-unity power factor.

from where it is clear that the generated virtual capacitance does cancel the effects of the filter inductance regarding the lowfrequency behavior of the system. Therefore, theoretical unity power factor is achieved.

The capability of bidirectional inverters to emulate virtual negative inductances has been proved in other applications [19], [20]. Therefore, another implementation possibility for the proposed APF control is to replace the virtual capacitance with a virtual negative inductance. This is derived from the idea given by the mains-side equivalent circuit analysis producing a series capacitance.

The according control diagram implementation is shown in Fig. 6, where

$$k_3 = \frac{-L_F}{V_c^* R_s}. \quad (22)$$

Such a control method is equivalent in many aspects to the virtual capacitance method. However, since it employs a differentiation block, it tends to present faster dynamics and is more prone to electromagnetic noise interference. Furthermore, the stability aspects are different as presented in Section III-C. The duty-cycle equation is then

$$d_F = \frac{R_s V_c^* \bar{i}_s}{v_m \bar{v}_c} - \frac{L_f}{\bar{v}_c} \frac{d\bar{i}_s}{dt}. \quad (23)$$

The generation of virtual impedances can be used to insert reactive power to the grid. This is done by deliberately changing parameters k_1 , k_2 , or k_3 at each of the control strategies. The effect is the emulation of a larger or smaller virtual impedance.

B. Equivalent-Feedback-Control-Based Analysis

The proposed control methods do not present an explicit current loop control. The current control is actually implicit in the control laws (12), (18), and (23) that determine the APF duty cycle. This is understood in the following. A classic feedback control loop is shown in Fig. 7, where $C(s)$ represents a current controller, $G(s)$ is the system model, and $H(s)$ is the transfer function of the measurement chain. The derivation in the following shows the equivalence between the proposed control methods and a conventional feedback control loop assuming that both are in steady state with a

constant dc-link voltage $v_c = V^* c$. Finally, the large-signal models are linearized around an operation point. Analyzing Fig. 7 results in the current controller being

$$C(s) = \frac{1}{\left(\frac{\tilde{i}_s^*}{\tilde{i}_s} - 1\right) \cdot G(s)} \quad (24)$$

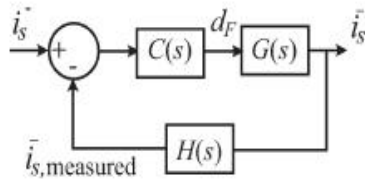


Fig. 7. Current control closed loop.

and the transfer functions I^*/I_s and $G(s)$ must be found for the proposed APF control strategies.

The loop equation of the circuit in Fig. 2 is

$$\bar{v}_s - L_F \frac{d\bar{i}_s}{dt} - R_L \bar{i}_s = d_F \bar{v}_C \quad (25)$$

where RL represents the inductor parasitic resistance. The current reference is given by

$$\tilde{i}_s^* = \frac{v_s}{R_e} \quad (26)$$

where R_e is the actual emulated resistance.

Assuming that v_s is sinusoidal and considering that i_s is proportional to it, it follows that

$$\frac{d\bar{i}_s}{dt} = -\omega_1^2 \int \bar{i}_s dt. \quad (27)$$

To obtain a single equation that represents the control system, (26) and (27) are replaced in (25), neglecting RL and resulting in

$$R_e \bar{i}_s + L_F \omega_1^2 \int \bar{i}_s dt = d_F \bar{v}_C. \quad (28)$$

Subtracting (25) from (28) gives

$$\bar{v}_s - L_F \frac{d\bar{i}_s}{dt} = R_e \bar{i}_s + L_F \omega_1^2 \int \bar{i}_s dt. \quad (29)$$

Linearizing (29) produces

$$L_F \tilde{I}_s = \tilde{R}_e I_{s,0} + R_{e,0} \tilde{I}_s + \frac{\omega_1^2 L_F \tilde{I}_s}{s} \quad (30)$$

where $\tilde{\cdot}$ represents the linearized variable and subscript 0 denotes the operating point. The linearization of (26) leads to

$$\tilde{R}_e = -\tilde{I}_s \frac{R_{e,0}}{I_{s,0}}. \quad (31)$$

Replacing (31) in (30) gives the linearized transfer function from the measured current to the reference current

$$\frac{\tilde{I}_s^*}{\tilde{I}_s} = \frac{s^2 + \frac{s}{\tau_e} + \omega_1}{\frac{s}{\tau_e}} \quad (32)$$

with $e = LF/Re,0$.

The next step is to find the plant function $G(s)$. This is obtained with the linearization of (25). Thus

$$G(s) = \frac{\tilde{I}_s}{\tilde{d}_F} = \frac{V_c^*}{R_L} \frac{1}{1 + \tau_L s} \quad (33)$$

with $L = LF/RL$.

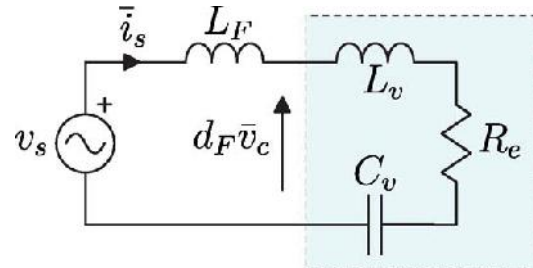


Fig. 8. Equivalent circuit for the control strategy to emulate both virtual

capacitance C_v and negative inductance L_v .

Finally, substituting (32) and (33) in (24) gives the equivalent implicit current controller $C_{implicit}(s)$ transfer function

$$C_{implicit}(s) = \frac{R_e}{V_o} \cdot \frac{s(s + \frac{1}{\tau})}{s^2 + \omega_1^2} \quad (34)$$

which shows the transfer function of a resonant controller tuned at 1. Resonant controllers in current control give excellent results with purely sinusoidal references [21]. The high gain at the tuned frequencies guarantees the reference follow-up and the rejection of components in other frequencies. In the proposed methods, the implicit resonant controller is implemented in a much simpler way than with the conventional control methods. Moreover, it follows from (34) that the bandwidth of the controller varies with the fundamental frequency ω_1 and the values of the circuit parameters R_e and LF . Similar results are found for the equivalent input current sensorless case.

C. Stability Analysis

The proposed control strategies given by (18) and (23) can be combined to analyze both options simultaneously and, in an implementation, to gain advantage from both sides. This strategy includes the integral (virtual capacitance) and derivative (virtual inductance) portions. This strategy gives

$$d_F \bar{v}_C = \bar{i}_s R_e + (L_s + L_v) \frac{d\bar{i}_s}{dt} + \frac{1}{C_v} \int \bar{i}_s dt \quad (35)$$

where C_v and L_v are the emulated (virtual) capacitance and inductance, respectively. These are computed to result in

$$jX_L - jX_C = j\omega(L_F - L_v) - j\frac{1}{\omega C_v} = 0. \quad (36)$$

Thus, it guarantees zero mains current phase displacement. This system generates the equivalent circuit shown in Fig. 8, which is used in the following stability analysis.

The transfer function from the mains voltage to the current in Fig. 8 is found as

$$\frac{\tilde{I}_s(s)}{\tilde{V}_s(s)} = \frac{s}{s^2(L_F + L_v) + sR_e + 1/C_v}. \quad (37)$$

The poles from the system modeled with (37) are

$$p_{system} = \frac{-R_e \pm \sqrt{R_e^2 - 4(L_F + L_v)/C_v}}{2(L_F + L_v)}. \quad (38)$$

Assuming positive R_e , i.e., power flow from the mains toward the load, and positive C_v , i.e., a capacitance to cancel

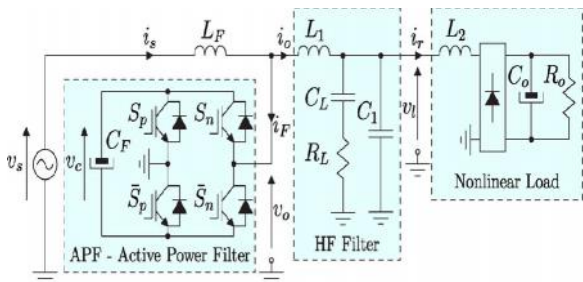


Fig. 9. APF power stage setup used both in the simulations and in the experimental results.

the effects of the APF inductance L_F , the system poles are in the right half-plane if

$$L_{eq} = L_F + L_v > 0. \quad (39)$$

Therefore, the first stability criterion is that the total series equivalent inductance is positive. This prevents the emulation of a pure negative inductance because, if $L_v = -L_F$, the system is oscillatory. A practical implementation would require either a pure virtual capacitance or a combination with a negative inductance so that (39) is met.

Still, from (38), the system presents damped oscillatory responses if

$$\frac{R_e}{4} < \frac{L_F + L_v}{C_v} \quad (40)$$

where $R_e = v_s^2 / P_o$ depends on the load power.

IV. SIMULATION RESULTS

The power stage configuration used in the simulation-based analysis of the proposed APF system is shown in Fig. 9. A remarkably low APF switching frequency of $f_c = 5$ kHz is used to highlight the performance of the proposed concepts. Other experimental parameters are as follows: The input ac voltage is set to $V_{s,rms} = 110$ V, mains frequency $f_s = 60$ Hz, APF inductance $L_F = 12.83$ mF, HF filter inductance $L1 = 1.4$ mH, HF filter resistance $R_L = 2$, HF filter capacitance $C_L = 8$ μ F, and HF filter capacitance $C1 = 0$ μ F (not used in this implementation). These setup parameters were chosen to approach the experimental setup in Section V. The nonlinear load is a single-phase diode bridge rectifier with the following parameters: $R_o = 40$, $C_o = 940$ μ F, and $L2 = 1$ mH.

The simulation results are shown in Figure.

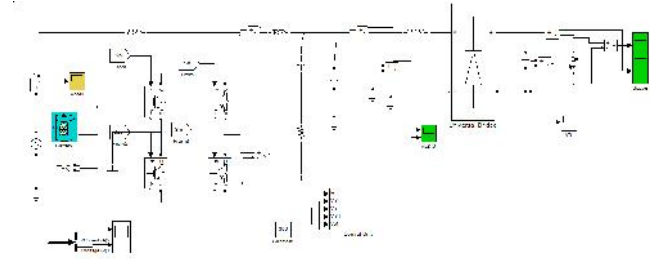


Fig. 10. Proposed APF with Battery

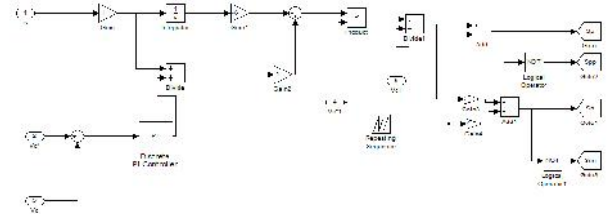


Fig. 11. Proposed Control Block.



Fig. 12. Source Current.

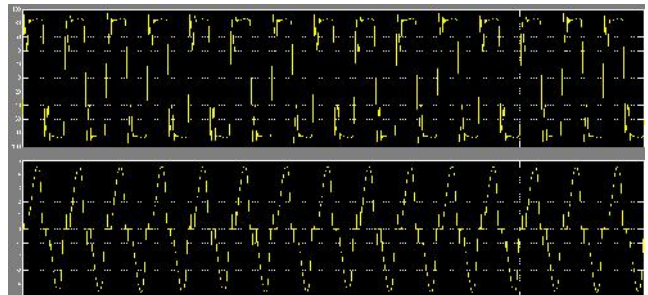


Fig. 13. VL & I0

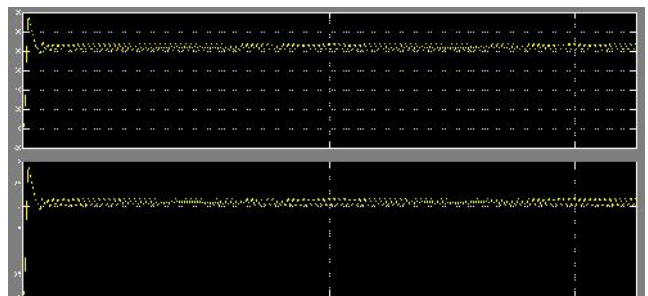


Fig.14. R-L Load Voltage & Current

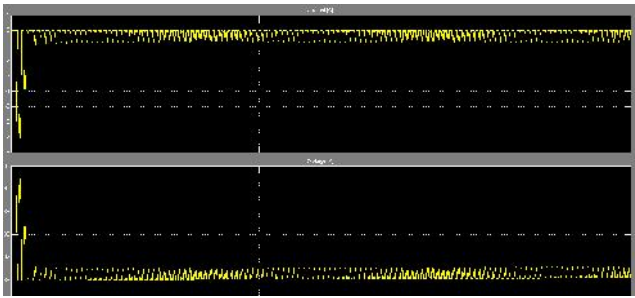


Fig. 15. Battery current & voltage

VI. CONCLUSION

Novel control strategies for a modified shunt APF architecture have been proposed here. The proposed strategies were able to guarantee close-to-unity power factor. Both current and voltage sensorless versions have been presented, where the voltage sensorless control has been analyzed in detail regarding its performance, equivalent circuits, and stability.

The main feature of the strategies is their extreme simplicity since no complex current reference computations are required. The implicit control loop is another innovative characteristic.

In this sense, it was proven that the proposed strategies are equivalent to explicit current control strategies employing a resonant-type controller. This explains the excellent sinusoidal tracking performance. In addition to the resistive behavior, the APF emulates virtual capacitance and/or negative inductance. Thus, zero mains-side current phase displacement is achieved.

These characteristics were verified through circuit simulation and in an experimental setup including a nonlinear rectifier load, with the APF being switched at 5 kHz. This is a very low switching and highlights the achievable performance. The concepts can be easily extended to the control of PFC rectifiers and three-phase systems.

REFERENCES

- [1] M. Cirrincione, M. Pucci, G. Vitale, and A. Miraoui, "Current harmonic compensation by a single-phase shunt active power filter controlled by adaptive neural filtering," *IEEE Trans. Ind. Electron.*, vol. 56, no. 8, pp. 3128–3143, Aug. 2009.
- [2] P. Salmeron and S. Litran, "Improvement of the electric power quality using series active and shunt passive filters," *IEEE Trans. Power Del.*, vol. 25, no. 2, pp. 1058–1067, Apr. 2010.
- [3] H. Akagi, A. Nabae, and S. Atoh, "Control strategy of active power filters using multiple voltage-source PWM converters," *IEEE Trans. Ind. Appl.*, vol. IA-22, no. 3, pp. 460–465, May 1986.
- [4] Y. Tang, P. C. Loh, P. Wang, F. H. Choo, F. Gao, and F. Blaabjerg, "Generalized design of high performance shunt active power filter with output LCL filter," *IEEE Trans. Ind. Electron.*, vol. 59, no. 3, pp. 1443–1452, Mar. 2012.
- [5] H. Akagi and K. Iozaki, "A hybrid active filter for a three-phase 12-pulse diode rectifier used as the front end of a medium-voltage motor drive," *IEEE Trans. Power Electron.*, vol. 27, no. 1, pp. 69–77, Jan. 2012.
- [6] M. Aredes, J. Hafner, and K. Heumann, "Three-phase four-wire shunt active filter control strategies," *IEEE Trans. Power Electron.*, vol. 12, no. 2, pp. 311–318, Mar. 1997.
- [7] S. Rahmani, N. Mendalek, and K. Al-Haddad, "Experimental design of a nonlinear control technique for three-phase shunt active power filter," *IEEE Trans. Ind. Electron.*, vol. 57, no. 10, pp. 3364–3375, Oct. 2010.
- [8] M. Routimo, M. Salo, and H. Tuusa, "Current sensorless control of a voltage-source active power filter," in *Proc. 20th Annu. IEEE APEC*, Mar. 2005, vol. 3, pp. 1696–1702.
- [9] M. Salo, "AC current sensorless control of the current-source active power filter," in *Proc. IEEE 36th PESC*, Jun. 2005, pp. 2603–2608.
- [10] D. Wojciechowski, "Sensorless predictive control of three-phase parallel active filter," in *Proc. AFRICON*, Sep. 2007, pp. 1–7.
- [11] G.-Y. Jeong, T.-J. Park, and B.-H. Kwon, "Line-voltage-sensorless active power filter for reactive power compensation," *Proc. Inst. Elect. Eng.—Elect. Power Appl.*, vol. 147, no. 5, pp. 385–390, Sep. 2000.
- [12] L. Dixon, "Average current mode control of switching power supplies," in *Proc. Nitrode Power Supply Semin.*, Sep. 1999, pp. 3-356–3-369.
- [13] A. Bhattacharya and C. Chakraborty, "A shunt active power filter with enhanced performance using ANN-based predictive and adaptive controllers," *IEEE Trans. Ind. Electron.*, vol. 58, no. 2, pp. 421–428, Feb. 2011.
- [14] H. Akagi and A. Nabae, "The p–q theory in three-phase systems under non-sinusoidal conditions," *Eur. Trans. Elect. Power*, vol. 3, no. 1, pp. 27–31, Jan./Feb. 1993.
- [15] E. Watanabe, H. Akagi, and M. Aredes, "Instantaneous p–q power theory for compensating nonsinusoidal systems," in *Nonsinusoidal Currents and Compensation, 2008. ISNCC 2008. International School on*, 2008, pp. 1–10.
- [16] E. Watanabe and M. Aredes, "Power quality considerations on shunt/series current and voltage conditioners," in *Proc. 10th Int. Conf. Harmon. Quality Power*, 2002, vol. 2, pp. 595–600.
- [17] M. Aredes and E. Watanabe, "New control algorithms for series and shunt three-phase four-wire active power filters," *IEEE Trans. Power Del.*, vol. 10, no. 3, pp. 1649–1656, Jul. 1995.
- [18] S. Rahmani, A. Hamadi, and K. Al-Haddad, "A Lyapunov-function-based control for a three-phase shunt hybrid active filter," *IEEE Trans. Ind. Electron.*, vol. 59, no. 3, pp. 1418–1429, Mar. 2012.
- [19] A. Borre, R. Dias, A. de Lima, and E. Watanabe, "Synthesis of controlled reactances using VSC converters," in *Proc. IEEE COBEP*, 2009, pp. 431–437.
- [20] A. Morsy, S. Ahmed, P. Enjeti, and A. Massoud, "An active damping

technique for a current source inverter employing a virtual negative inductance,” in *Proc. 25th Annu. IEEE APEC*, 2010, pp. 63–67.

[21] F. Blaabjerg, R. Teodorescu, M. Liserre, and A. Timbus, “Overview of control and grid synchronization for distributed power generation systems,” *IEEE Trans. Ind. Electron.*, vol. 53, no. 5, pp. 1398–1409, Oct. 2006.

[22] M. L. Heldwein, “EMC filtering of three-phase PWM converters,” Ph.D. dissertation, ETH Zürich, Zürich, Switzerland, 2008.